Reaction paths and kinetics of aluminide formation in Al/epitaxial-W(001) model diffusion barrier systems

D. B. Bergstrom, I. Petrov, L. H. Allen, and J. E. Greene
Coordinated Science Laboratory, Materials Research Laboratory, and Department of Materials Science, 1101 West Springfield, University of Illinois, Urbana, Illinois 61801

(Received 5 December 1994; accepted for publication 23 February 1995)

Single-crystal bcc W(001) layers, 140 nm thick, were grown on MgO(001) substrates by ultrahigh-vacuum (UHV) magnetron sputter deposition at $T_s = 600$ °C. Al overlayers, 190 nm thick with strong (001) and (011) preferred orientation and an average grain size of 200 nm, were then deposited at $T_s = 100$ °C without breaking vacuum. Changes in bilayer sheet resistance R_s were monitored continuously as a function of time t_a and temperature T_a during UHV annealing. In addition, Rutherford backscattering spectroscopy, x-ray diffraction, transmission electron microscopy (TEM), and scanning TEM, in which cross-sectional specimens were analyzed by energy-dispersive x-ray analysis with a 1 nm resolution, were used to follow area-averaged and local interfacial reaction paths as well as microstructural changes as a function of annealing conditions. The initial reaction products were discontinuous regions of monoclinic-structure WAl_4 which exhibit a crystallographic relationship with the underlying W layer. bcc WAl_{12} forms at a later stage and grows conformally to cover both W and WAl_4. WAl_4 and WAl_{12} continue to grow, with W being the primary mobile species, until the Al layer is completely consumed. Information from the microchemical and microstructural analyses was used to model the $R_s(T_a, t_a)$ results based upon a multielement equivalent circuit approach which accounts for the observed nonplanar nature of the reaction front. Reaction kinetics and activation energies were determined. The results show that the growth of WAl_4 is diffusion limited with an activation energy E_a of 3.1 eV while the formation of WAl_{12} is reaction limited with $E_a = 3.3$ eV. © *1995 American Institute of Physics.*

I. INTRODUCTION

As the dimensions of integrated circuits continue to decrease while the number of heterointerfaces increase, it becomes increasingly important to understand the microchemical and microstructural interfacial reaction paths affecting the integrity of, for example, layers used in applications such as diffusion barriers. W and Ti_xW_{1-x} alloys, where Ti is added to increase adhesion and improve corrosion resistance,[1] are presently used as diffusion barriers between Si (or silicide, SiO_2, or Si_3N_4) layers and Al contacts in order to inhibit Al spiking and/or interfacial chemical reactions during subsequent high-temperature processing steps in device fabrication.[2] The failure of polycrystalline TiW diffusion barriers has been widely investigated in multilayer metallization schemes including: Al/TiW/SiO_2;[3–9] Al/TiW/Si;[10–12] Al/TiW/silicide/Si;[13–17] and Al/TiW/Si_3N_4/Si.[18] Many of these studies are discussed in a recent review article on aluminide formation.[19] The bulk of this work suggests that barrier failure occurs, depending on the details of sample preparation, at annealing temperatures T_a between 400 and 550 °C. Several barrier failure mechanisms have been proposed: diffusion of Al through TiW grain boundaries;[12,13] diffusion of Ti through Al to the surface of the film where it forms Al_3Ti;[4,18] diffusion of W through Al grain boundaries;[16] and interfacial reactions to form one or more of the stable tungsten aluminides: WAl_{12},[5–10,13,18,20] WAl_5,[5–7,9] and WAl_4.[6,9,18]

In the case of Al/W interactions, presently available evidence suggests that failure of polycrystalline W barriers begins to occur at somewhat higher temperatures, T_a between[20–24] 500 and 550 °C for an annealing time, $t_a = 0.5$ h. Wang and Mayer[23,24] carried out marker experiments in which a 3-nm-thick Ni layer deposited between the Al and W layers was observed, after annealing, at the Al aluminide interface. They concluded that the mobile species is therefore Al. The evidence, however, is not conclusive. The bilayers were analyzed only by Rutherford backscattering spectroscopy (RBS); no transmission electron microscopy (TEM) analyses were reported. Thus, it is unknown whether the as-deposited marker layer was islanded (the desired case) or continuous or even whether the Ni layer was "inert" in the reaction. Moreover, it is possible that W is actually the dominant diffusing species in the bilayer couple while Ni segregates to the free Al surface in a manner similar to that which has been reported for Ti in Al/TiW bilayer reactions.[4,18]

Relatively little is known concerning microstructural and local, rather than area-averaged, microchemical reaction paths during annealing of Al/W and Al/TiW thin-film couples. RBS analyses of reacted Al/W bilayers have demonstrated that the reaction front is nonplanar.[20] Similarly, the few cross-sectional TEM (XTEM) results that have been reported for annealed Al/TiW bilayers show highly nonplanar reacted zones.[6,9] The formation of other transition-metal (including Hf, Zr, and Ta) aluminides is also known to proceed through a nonplanar reaction front.[25] This makes the interpretation of kinetic data difficult and is probably responsible in large part for the lack of definitive reaction kinetics studies on these systems.

In this article we present the initial results of investigations, including both experiments and modeling, aimed at understanding the detailed reaction paths and kinetics of the

 0021-8979/95/78(1)/194/10/$6.00 © 1995 American Institute of Physics

Downloaded 30 May 2001 to 130.126.103.205. Redistribution subject to AIP license or copyright, see http://ojps.aip.org/japo/japcr.jsp

initial stages of Al/W interfacial reactions. The present experiments were carried out using Al/single-crystal-W(001) bilayers, grown by ultrahigh vacuum (UHV) magnetron sputter deposition on MgO(001). W barrier layers were chosen in order to focus first on bulk interfacial reactions without the additional complexity associated with the presence of Ti. The use of epitaxial W(001) also eliminates potential competing reaction paths such as Al diffusion through W grain boundaries. The bilayer sheet resistance, R_s was monitored continuously as a function of time t_a and temperature T_a during UHV annealing. In addition, RBS, TEM, and scanning TEM (STEM), in which cross-sectional specimens were analyzed by energy-dispersive x-ray analysis (EDX) with a 1 nm resolution, were used to follow area-averaged and local interfacial reaction paths as well as microstructural changes as a function of annealing conditions. The microchemical and microstructural data were then used to model $R_s(t_a)$, accounting for the nonplanar reaction front, in order to determine reaction kinetics and activation energies. The results of these analyses show that the first phase to form is WAl_4, exhibiting diffusion-limited three-dimensional growth with an activation energy of 3.1 eV. WAl_{12} forms later with reaction-rate-limited kinetics and an activation energy of 3.3 eV.

II. EXPERIMENTAL PROCEDURE

All Al/W bilayers were grown in a load-locked multichamber UHV stainless-steel dc magnetron sputter-deposition system which has been described in detail elsewhere.[26–28] The pressure in the sample introduction chamber was reduced to less than 5×10^{-8} Torr (7×10^{-6} Pa) using a 50 $\ell\,s^{-1}$ turbomolecular pump (TMP) before initiating substrate exchange with the deposition chamber which has a base pressure of 5×10^{-10} Torr (7×10^{-8} Pa), achieved using a 500 $\ell\,s^{-1}$ TMP. For the present experiments, an additional magnetron sputtering source, with separate water cooling lines and shutter, was added in the viewport flange opposing the original source. Both sources were operated in a magnetically balanced mode.[27] The targets were 7.6-cm-diam, 4-mm-thick, solid W (99.95% pure) and 6.4-cm-diam by 4 mm Al (99.999%) disks. Target-to-substrate separations were 6.5 cm for W and 10 cm for Al deposition.

The primary substrates used in these experiments were cleaved $1\times1\times0.1$ cm^3 MgO(001) wafers. Substrate cleaning and degreasing consisted of successive rinses in ultrasonic baths of trichloroethylene, acetone, ethanol, and de-ionized water. The wafers were then blown dry in dry N_2 immediately prior to inserting them into the load-lock chamber for transport to the growth chamber. The MgO wafers were mounted on resistively heated Ta platens using Mo clips. A 0.25-mm-diam Chromel-Alumel thermocouple, bonded to a dummy MgO wafer using Ag paste, was used to calibrate the substrate temperature T_s before and after the growth experiments. The substrates were thermally degassed at 800 °C for 1 h which was shown in a separate UHV apparatus to provide sharp 1×1 reflection high-energy electron-diffraction patterns.[29] The substrate temperature controller was then adjusted to the W growth temperature, 600 °C, while the target was sputter cleaned for 5 min with the substrate shielded by a rotatable shutter. Reported T_s values include the contribution from plasma heating.

Sputtering was carried out in 99.999% pure Ar injected into the deposition chamber through a high-precision solenoid valve. A capacitance manometer with an automatic mass-flow controller was used to maintain the Ar pressure constant during deposition. W films, 140 nm thick, were deposited at $T_s=600$ °C in a 15 mTorr (2.0 Pa) Ar discharge sustained using a constant-current dc power supply operated at 0.53 A and 167 W which resulted in a film deposition rate of 87.5 nm min^{-1}. Following W deposition, T_s was decreased to 50 °C, and a 190-nm-thick Al layer was deposited in a 5 mTorr (0.67 Pa) 167 W Ar discharge at 0.4 A yielding an Al deposition rate of 84.5 nm min^{-1}. T_s increased to 100 °C during Al deposition due to plasma heating. The samples were allowed to cool to $T_s<50$ °C before transferring them to the load-lock chamber which was then vented with dry N_2.

As-deposited samples were annealed using both linear temperature ramps and isothermal soaks at temperatures T_a up to 550 °C in an UHV furnace with a base pressure of 5×10^{-8} Torr (6.6×10^{-6} Pa). During annealing, the bilayer sheet resistance R_s was measured *in situ* using a four-point probe consisting of spring-loaded Mo probes arranged in a van der Pauw geometry.[30] Resistance and temperature data were recorded by computer every 20 s.

The microstructure and microchemistry of both as-deposited and annealed samples were determined using a combination of RBS, XRD, TEM, XTEM, STEM, and EDX. The RBS probe beam consisted of 2 MeV He^+ ions incident at an angle of 22.5° relative to the sample surface normal with the detector set at a 30° scattering angle. Backscattered spectra were analyzed using the RUMP simulation program.[31] The XRD system was operated with Cu$K\alpha$ radiation and was equipped with a double-crystal spectrometer to provide a resolution of 0.01 ° 2θ. XRD analyses were carried out in both the crystal diffraction mode (20 kV, 2 mA, and 0.05° divergent slit) and in the powder-diffraction mode (45 kV, 20 mA, 1° divergent slit).

A Philips CM 12 microscope with a LaB_6 filament operated at 120 kV was used for plan-view and XTEM analyses. Plan-view specimens were prepared by first mechanically thinning them from the back side with SiC to a thickness of $\simeq$40 μm. Final thinning to electron transparency was accomplished by ion milling using a 5 kV, 1 mA, Ar^+-ion beam incident initially at 15° and then decreased to 12°. XTEM samples were cleaved into slabs approximately 1 mm thick and mechanically thinned and ion milled from both sides. Due to the difference in sputtering yields between the metal layers and the MgO substrate, ion etching was always done with the film side of the sample facing away from the ion beam. EDX analyses of XTEM samples were performed in a Vacuum Generators HB5 STEM equipped with a field-emission source operated at 100 kV. The samples were probed with a stationary electron beam focused to a diameter of 1 nm, and x-ray spectra were collected at a takeoff angle of 40°. Corrections for atomic number were carried out using the MAGIC-V program;[32] however, due to the thickness of the

Downloaded 30 May 2001 to 130.126.103.205. Redistribution subject to AIP license or copyright, see http://ojps.aip.org/japo/japcr.jsp

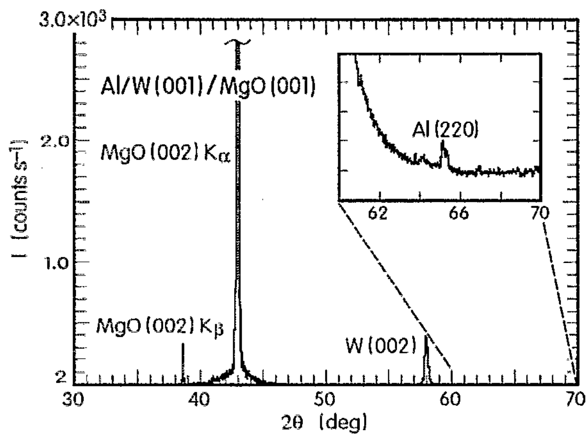

FIG. 1. $\theta-2\theta$ single-crystal-mode XRD pattern from an as-deposited Al/W(001) bilayer. The inset shows a θ-2θ powder scan containing the Al (220) peak.

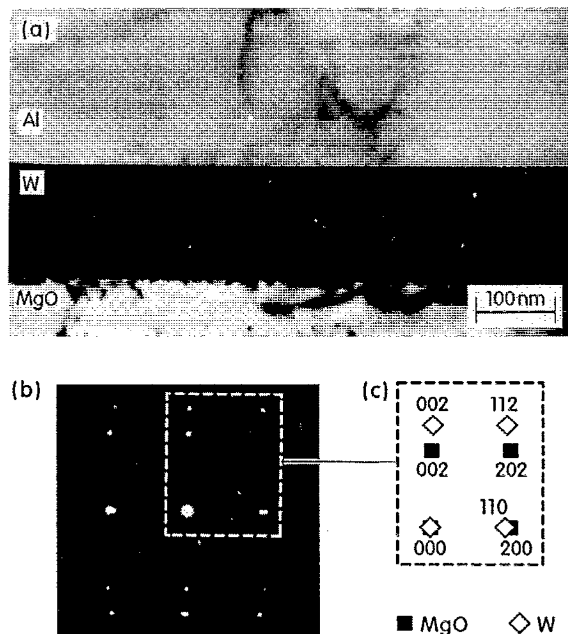

FIG. 2. (a) Bright-field XTEM micrograph and (b) the corresponding SAED pattern from an as-deposited Al/W(001) bilayer. A simulated diffraction pattern is shown in (c).

XTEM samples, <50 nm, corrections for absorption and fluorescence were insignificant.

III. EXPERIMENTAL RESULTS

A. As-deposited Al/W(001) bilayers

A double-crystal XRD pattern from an as-deposited Al/W bilayer grown on MgO(001) is shown in Fig. 1. The W and substrate peaks observed over the range of 2θ scanned, 10°–70°, were the MgO (002) $K\alpha_1$ and $K\alpha_2$ at 42.89° and 43.02° 2θ, the MgO (002) $K\beta$ at 38.59° 2θ, and the W (002) $K\alpha_1$ and $K\alpha_2$ at 57.93° and 58.07° 2θ. The lattice parameter a_W of the W film was found to be 0.3184 nm, slightly larger than the bulk value of 0.316 48 nm.[33] Thus, the film is mostly relaxed with some residual in-plane compression. The Al (220) peak at 65.10° 2θ was the only Al peak not obscured by a substrate peak and its position is in agreement with that expected from bulk Al indicating that the layer is relaxed.

Figure 2(a) shows a typical XTEM micrograph from an as-deposited Al/W bilayer structure together with a corresponding selected-area electron-diffraction (SAED) pattern, Fig. 2(b), obtained using a 0.5 μm aperture centered on the W/MgO interface. Al and W layer thicknesses determined from XTEM micrographs were found to be 190 and 140 nm, respectively, in good agreement with values expected from deposition rate calibrations. W/MgO and Al/W interfaces were smooth and abrupt with the only contrast being that due to strain associated with lattice misfit. Grain boundaries were only observed in the Al overlayer. The simulated electron-diffraction pattern shown in Fig. 2(c) demonstrates that the epitaxial relationship between W and the MgO substrate is W[001]‖MgO[001] with W[110]‖MgO[100]. Thus, the bcc W lattice is rotated 45° about the [001] growth axis with respect to the NaCl-structure MgO substrate (a_{MgO}=0.4213 nm)[33] as observed previously.[34] This rotation reduces the lattice misfit $(a_W-a_{MgO})/a_{MgO}$ from 24.9% tension for an in-plane W[100]‖MgO[100] orientation to 6.2% compression with the observed orientation. The film/substrate epitaxial relationship is thus controlled by the strain component of the total system free energy.

A typical bright-field plan-view TEM micrograph from an as-deposited Al/W bilayer is shown in Fig. 3(a) with corresponding SAED and simulated patterns, Figs. 3(b) and 3(c). The MgO and W have been milled away in this portion of the sample, leaving only the Al. Figure 3(a) shows that the Al layer is polycrystalline with an average grain size of 200 nm. The SAED pattern in Fig. 3(b) is a composite of a [001] and two 90°-rotated [011] zone-axis patterns indicating that the Al grains grow with three strongly preferred orientations. Grains corresponding to the [001] zone axis are rotated 45° with respect to the W layer so that Al[100]‖W[110] and Al[110]‖W[010]. Using the bulk Al lattice constant, a_{Al}=0.404 94 nm,[33] the measured lattice constant in the growth direction of the partially relaxed W layer, and the Poisson ratio for W, ν=0.280,[35] the in-plane mismatch is 8.8% tensile. Grains corresponding to the [011] zone axes have the in-plane orientation relationship Al[100]‖W[010] and Al[01$\bar{1}$]‖W[100] with lattice misfits of 27.9% compression and 8.8% tension, respectively.

B. Annealed Al/W(001) bilayers

Al/W(001) bilayer structures were annealed at temperatures between 450 and 550 °C. A typical plot of normalized sheet resistance R_s/R_s^0, vs t_a for T_a=475 °C is shown in Fig. 4. The overall shapes of all $R_s(t_a)$ isothermal annealing curves were quite similar. R_s initially increases rather slowly and then more rapidly before finally bending over toward saturation after an overall increase by a factor of approximately 4.

Downloaded 30 May 2001 to 130.126.103.205. Redistribution subject to AIP license or copyright, see http://ojps.aip.org/japo/japcr.jsp

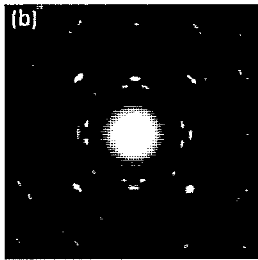

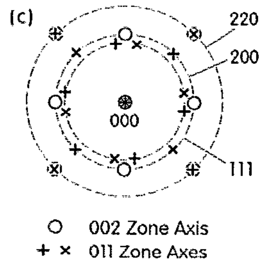

FIG. 3. (a) Bright-field plan-view TEM micrograph and (b) the corresponding SAED pattern from an as-deposited Al/W(001) bilayer in which the W layer has been removed by ion milling. A simulated diffraction pattern is shown in (c).

Bilayer $R_s(t_a)$ isothermal annealing results corresponding to interfacial reactions between two or more layers are typically analyzed using a parallel resistor model in which the measured sheet resistance is the inverse of the sum of the inverse sheet resistances of each of the layers in the structure.[36] This can be expressed more straightforwardly in terms of sheet conductances, $G_s=1/R_s$, where the measured sheet conductance of the reacted bilayer is

$$G_s=R_s^{-1}=\sum_i \sigma_i z_i. \tag{1}$$

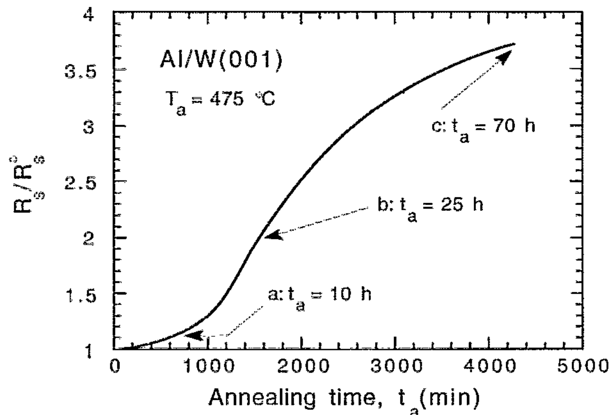

FIG. 4. Normalized sheet resistance R_s/R_s^0 vs time t_a during UHV isothermal annealing of an Al/W(001) bilayer at $T_a=475$ °C.

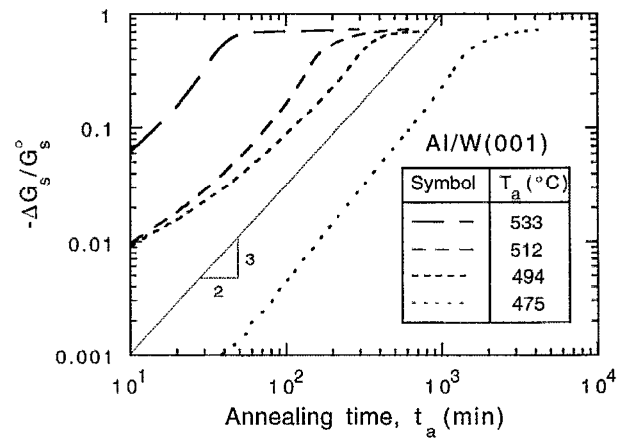

FIG. 5. log-log plot of the normalized decrease in sheet conductivity $-\Delta G_s/G_s^0$ as a function of time t_a during UHV annealing at $T_a=475$, 494, 512, and 533 °C.

σ_i and z_i in Eq. (1) are the conductivity and thickness, respectively, of layer i.

In the simple case of a bilayer for which all interfaces remain planar and the product phase is a line compound of fixed composition, the change in the measured sheet conductance ΔG_s is directly proportional to the thickness z_p of the product layer. Thus, the slope of time-dependent isothermal annealing data plotted as $\log(-\Delta G_s/G_s^0)$ vs $\log(t_a)$, where G_s^0 is the sheet conductance of the as-deposited bilayer, should be the same as that for $\ln(z_p)$ vs $\ln(t_a)$, which from thin-film theory[37] is unity for reaction-rate-limited kinetics or 0.5 for diffusion-limited kinetics. However, this analysis cannot be directly applied to our Al/W results as shown by the experimental $\log(-\Delta G_s/G_s^0)$ vs $\log(t_a)$ data in Fig. 5 obtained at annealing temperatures between 475 and 533 °C. The slopes of the intermediate rapidly varying regions of the curves are not in the range from 0.5 to 1 but, in fact, are close to 1.5 in all cases. The Al/W interfacial reaction path is clearly more complex than that described by the simple parallel-reaction-front model.

Figure 6 shows glancing-angle XRD patterns from an as-deposited bilayer as well as from samples annealed at $T_a=475$ °C to R_s/R_s^0 values of 1.14, 2.0, and 3.7 corresponding to the points labeled (a) $t_a=10$ h, (b) $t_a=25$ h, and (c) $t_a=70$ h, respectively, in Fig. 4. For these measurements the incident beam angle θ was chosen to be 2°, highly misaligned for Bragg diffraction from the MgO substrate, the epitaxial W(001) film, and the strongly textured Al grains, in order to provide minimum interference for detecting small peaks associated with reaction products. The XRD pattern obtained after 10 h of annealing at $T_a=475$ °C was essentially identical to that obtained from the as-deposited sample. The only peak observed, near 29° 2θ, emanated from the substrate holder. The glancing-angle XRD pattern obtained after 25 h of annealing, however, exhibits a peak near that expected for WAl_{12} (110), while the $t_a=70$ h pattern contains several reaction product peaks, all indexable to WAl_{12}. However, this does not of itself establish the absence of other phases that may be present with strong preferred orientations

Downloaded 30 May 2001 to 130.126.103.205. Redistribution subject to AIP license or copyright, see http://ojps.aip.org/japo/japcr.jsp

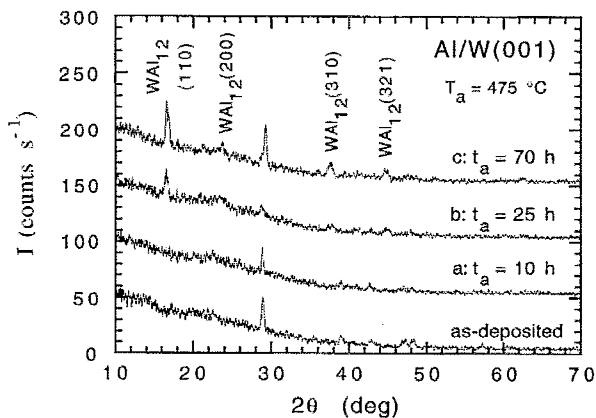

FIG. 6. Glancing-angle XRD patterns from an as-deposited Al/W(001) bilayer and bilayers annealed in UHV at T_a=475 °C for t_a=10, 25, and 70 h. The unlabeled peak near 2θ=29° emanates from the XRD sample holder.

such that their corresponding Bragg peaks are also misaligned.

RBS spectra from the same samples used to obtain the results presented in Fig. 6 are reproduced in Figure 7. The spectrum from the as-deposited bilayer shows, in agreement with the XTEM micrograph in Fig. 2(a), that the W and Al layers are abrupt and of uniform thickness. The leading edge of the W profile, just above 1.7 MeV, and the trailing edge of the Al profile, near 1.0 MeV, corresponding to the initial bilayer interface are sharp. After 10 h of annealing at 475 °C, the Al peak is relatively unchanged while the W peak has broadened toward higher energies indicating W penetration throughout the Al layer. The W surface concentration at this point is ≃0.2 at. %. It not possible to determine from such RBS spectra alone whether the W has dissolved into the Al to form a metastable supersaturated solid solution (the maximum Al equilibrium solid solubility at this temperature is 0.014 at. %),[38] is residing primarily in Al grain boundaries, or has reacted to form a tungsten aluminide phase. With further annealing, W continues to diffuse into the Al overlayer. In the t_a=25 h profile in Fig. 7, the shoulder on the high-energy side of the W peak has become more pronounced and advanced farther toward the free surface while the Al peak has begun to broaden toward lower energies. After annealing for t_a=70 h, interdiffusion has proceeded to the point where the W composition at the surface corresponds to that of WAl_{12}.

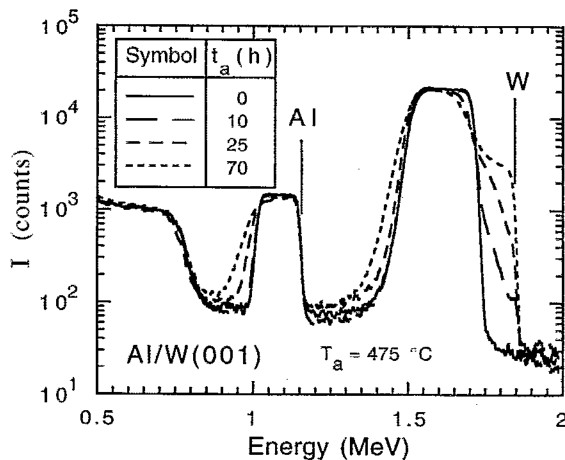

FIG. 7. RBS spectra from an as-deposited Al/W(001) bilayer and bilayers annealed in UHV at T_a=475 °C for t_a=10, 25, and 70 h.

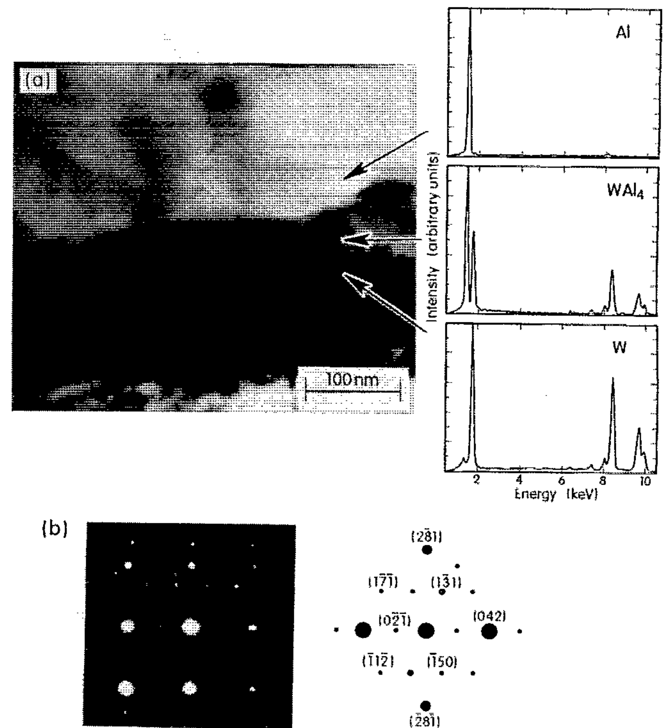

FIG. 8. (a) Bright-field XTEM micrograph from an Al/W(001) bilayer annealed at T_a=475 °C for t_a=10 h. Selected-area EDX spectra, obtained using a 1-nm-diam probe beam, from regions just above, within, and just below the reaction product phase are also shown. (b) A SAED pattern obtained from the reaction product phase and a corresponding computer-simulated WAl_4 $[51\bar{2}]$ zone-axis pattern.

Our RBS and XRD results are in substantial agreement with earlier studies[20–24] which relied almost exclusively on these two techniques, reporting that WAl_{12} is formed during 0.5 h anneals at temperatures as low as 500 °C. However, our XTEM analyses of partially reacted Al/W bilayer samples show in addition that interfacial reactions begin at local regions forming isolated grains which grow into the Al layer while the W surface remains planar. Figure 8(a) is an XTEM micrograph showing such a grain formed in a bilayer film annealed under conditions coinciding with position (a) in Fig. 4 (T_a=475 °C, t_a=10 h) and with the corresponding XRD and RBS results in Figs. 6 and 7, respectively. The grain, whose size is typical of most reaction-product grains observed at this stage of reaction, has a height of about 50 nm. The composition of the grain was determined from EDX results obtained in a STEM using a 1 nm probe beam. Spectra obtained from just above the reacted zone, within the grain, and just below the reacted zone are also shown in Fig. 8(a). The only peak obtained in the upper spectrum is the Al$K\alpha$ peak at 1.49 keV, while the lower spectrum exhibits only the W$L\alpha$, $L\beta$, $M\alpha$, and $M\beta$ peaks 8.3, 9.8, 1.77, and

Downloaded 30 May 2001 to 130.126.103.205. Redistribution subject to AIP license or copyright, see http://ojps.aip.org/japo/japcr.jsp

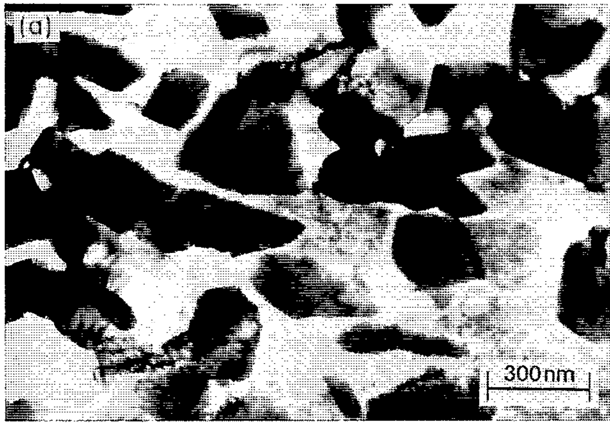

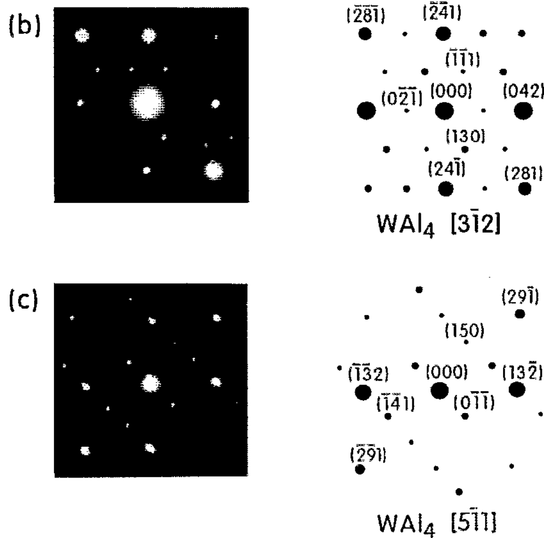

FIG. 9. (a) Bright-field plan-view TEM micrograph from an Al/W(001) bilayer annealed at T_a=475 °C for t_a= 10 h. (b) and (c) are SAED patterns obtained from WAl_4 grains with the two primary textures observed. Corresponding computer-simulated WAl_4 $[3\bar{1}2]$ and WAl_4 $[5\bar{1}1]$ zone-axis diffraction patterns are also shown.

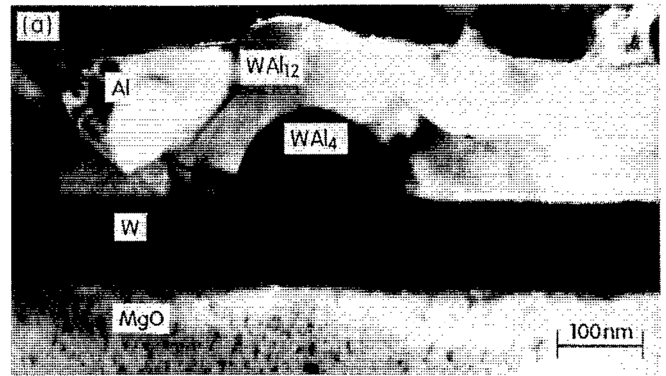

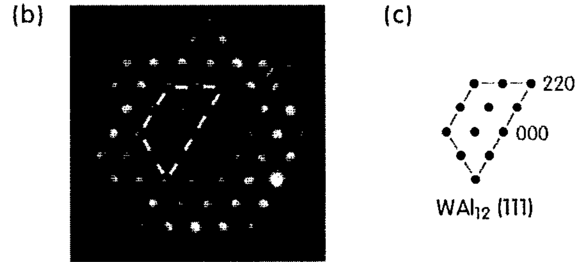

FIG. 10. (a) Bright-field XTEM micrograph from an Al/W(001) bilayer annealed at T_a=475 °C for t_a=25 h. (b) A convergent-beam SAED pattern obtained from the WAl_{12} reaction product phase together with (c) a simulated WAl_{12} [111] zone axis pattern.

1.84 keV, respectively. The middle spectrum from the reacted zone indicates the presence of both Al and W with an Al/W composition ratio of 4. An analysis of SAED patterns provides consistent results. All reflections can be indexed as monoclinic-structure WAl_4 (a_0=0.5272 nm, b_0=1.7771 nm, c_0=0.5218 nm, β=100°12′).[39] The SAED pattern in Fig. 8(b) was obtained with the electron beam oriented along the W $[1\bar{1}0]$ zone axis which corresponds to the WAl_4 $[51\bar{2}]$ zone axis as shown by comparison with the simulated diffraction pattern.

Figure 9(a) is a plan-view TEM micrograph of the same sample imaged in Fig. 8 showing that the WAl_4 grains are randomly distributed along the interfacial area. From an analysis of SAED patterns, there are two preferred WAl_4 grain orientations. Typical SAED patterns are shown in Figs. 9(b) and 9(c). Based upon comparisons with computer simulations [also shown in Figs. 9(b) and 9(c)], the patterns correspond to the $[3\bar{1}2]$ and $[5\bar{1}1]$ zone axes of WAl_4. The higher intensity of reflections such as (042), $(24\bar{1})$, and $(13\bar{2})$ in both the experimental and simulated patterns is due to the fact that these planes have higher atom number densities and hence larger structure factors. SAED patterns from samples containing both the WAl_4 and underlying W phases show that the high-intensity WAl_4 reflections are always aligned with W {110} reflections. Mismatches in interplanar spacing between the WAl_4 (042), $(24\bar{1})$, and $(13\bar{2})$ and W {110} planes are relatively small, −0.63%, +2.3%, and −2.3% respectively. Thus, the growth of the WAl_4 phase appears to be stabilized by a pseudomorphic relationship with the W underlayer. No evidence—by RBS, XRD, or STEM—was obtained for the presence of bcc-structure WAl_{12} at this stage in the reaction path.

Figure 10(a) is a XTEM micrograph of a sample annealed at 475 °C for 25 h corresponding to point (b) in Fig. 4. The WAl_4 grains have grown to a height of 100 nm corresponding to approximately half of the original Al/aluminide layer thickness. A new phase with brighter contrast (indicating the presence of a larger fraction of the lower mass constituent, Al) has also grown conformally along the interfaces between Al and W and between Al and WAl_4 with an approximately uniform thickness of ≃80 nm. A typical SAED pattern obtained from this layer is shown in Fig. 10(b) to match the simulated WAl_{12} [111] zone axis diffraction pattern in Fig. 10(c).

A XTEM micrograph from a film annealed for t_a=70 h with T_a=475 °C [point (c) in Fig. 4] is shown in Fig. 11. In this case, the original Al overlayer has been completely consumed. Comparing this micrograph with the one in Fig. 10(a), obtained after a 25 h anneal at 475 °C, shows that while the WAl_4 grains have continued to grow, the WAl_{12}

Downloaded 30 May 2001 to 130.126.103.205. Redistribution subject to AIP license or copyright, see http://ojps.aip.org/japo/japcr.jsp

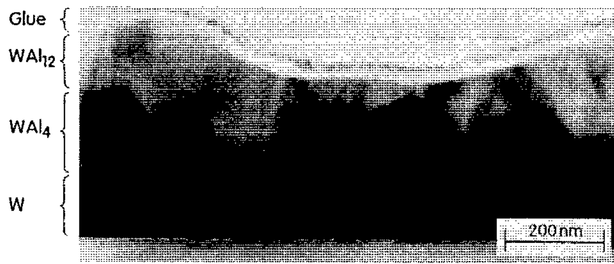

FIG. 11. Bright-field XTEM micrograph from an Al/W(001) bilayer annealed at $T_a = 475$ °C for $t_a = 70$ h.

layer remained conformal and grew at a much higher rate. This structure—a blanket coating over isolated WAl_4 grains—is reflected in the undulating surface topography of the fully reacted sample.

IV. DISCUSSION AND MODEL DEVELOPMENT

The results presented in Sec. III show that interfacial reactions in the Al/W(001) bilayer couple are complex and proceed through a nonplanar reaction front. The initial phase observed is monoclinic-structure WAl_4 which nucleates discontinuously along the interface, consuming Al grains, and grows with a texture influenced by that of the W underlayer. At a later stage, bcc-structure WAl_{12} nucleates both at the original Al/W interface between WAl_4 islands and at Al/WAl_4 interfaces. The WAl_{12} phase grows conformally and the reaction proceeds to consume the remaining Al through the continued growth of both aluminide phases.

It is frequently asserted in the literature, primarily based on the marker experiments discussed earlier, that Al is the primary diffusing species in Al/W thin-film reactions. We observe, however, that the surface of the W layer remains planar throughout the entire reaction (see, for example, the XTEM micrographs in Figs. 8, 10, and 11) in which the WAl_4 and WAl_{12} product phases nucleate and grow with a nonplanar interface into the Al layer. This was true for all samples analyzed irrespective of annealing temperature and is not consistent with W being immobile. Furthermore, the WAl_{12} phase grows over the WAl_4 phase without significantly altering the shape of the WAl_4 grains. These observations indicate that the moving interface for both aluminide phases is on the Al, rather than the W, side. This is clearly observed in the growth of WAl_{12} where the WAl_4 grains act as markers along the Al/W interface. Therefore, we conclude that W, not Al, is the primary mobile species in these experiments.

An early stage in the Al/W(001) bilayer reaction is shown schematically in Fig. 12(a). The sample consists of three separate layers: Al, a layer containing both WAl_4 and Al, and W. This can be represented by the parallel resistor equivalent circuit shown in Fig. 12(b) in which, as opposed to previous models (see, for example, Ref. 16), the resistivity of the intermediate layer depends in a complex manner on the amount and distribution of the product phase WAl_4. The overall sheet conductance can be expressed by Eq. (1) as the sum of the products of the layer conductivities and their thicknesses. The conductivities of layers 1 and 3 are just

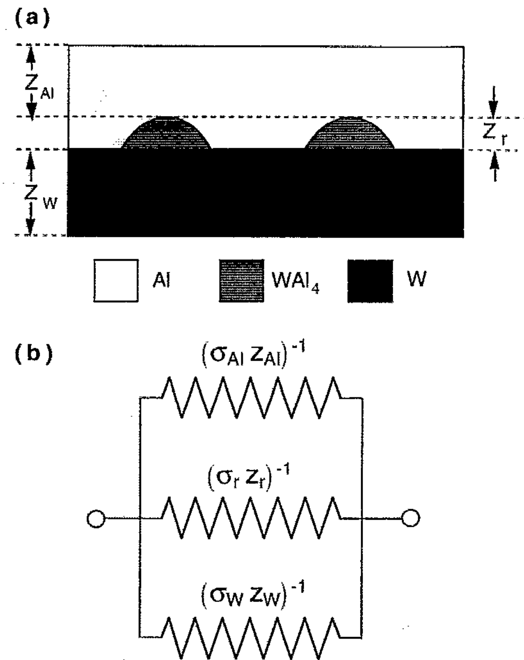

FIG. 12. (a) Schematic representation of the initial stages of WAl_4 product formation during annealing of Al/W(001) bilayers together with (b) an equivalent circuit representation in which σ and z are layer conductivities and thicknesses, respectively. The subscript r refers to the reacted layer.

those of pure Al and W. In the case of layer 2, however, the second phase nucleates discontinuously and grows into the Al layer. The conductivity of such a heterogeneous material can be approximated, assuming a random distribution of nucleation sites and using embedded network analysis, by the equation[40]

$$\sigma = \prod_j \sigma_j^{f_j}, \tag{2}$$

where σ_j and f_j are the conductivity and volume fraction, respectively, of phase j.

Substituting Eq. (2) into Eq. (1) yields an expression for the overall sheet conductance including all phases,

$$G_s = \sigma_{Al} z_{Al} + (\sigma_{Al}^{f_{Al}} \sigma_{WAl_4}^{f_{WAl_4}}) z_r + \sigma_W z_W, \tag{3}$$

where z_r is the thickness of the reacted layer. Thus,

$$\Delta G_s = \sigma_{Al} \Delta z_{Al} + (\sigma_{Al}^{f_{Al}} \sigma_{WAl_4}^{f_{WAl_4}}) z_r + \sigma_W \Delta z_W. \tag{4}$$

A common approximation to make at this point is to assume that the conductivity is dominated by one layer, Al in this case; however, we pursue a more general approach here since the resistivities of WAl_4 and WAl_{12} are unknown and may be similar to Al. Based upon primitive unit-cell sizes the total volume change upon the reaction of bcc W and fcc Al to form monoclinic WAl_4 is less than 2%, so the total thickness of the bilayer can be approximated as being constant during WAl_4 growth. Moreover, the thickness z_W of the W layer decreases in direct proportion to the volume of WAl_4 formed. Thus,

Downloaded 30 May 2001 to 130.126.103.205. Redistribution subject to AIP license or copyright, see http://ojps.aip.org/japo/japcr.jsp

$$\Delta z_{\mathrm{W}} = -V^* f_{\mathrm{WAl}_4} z_r,$$
$$\Delta z_{\mathrm{Al}} = -z_r + V^* f_{\mathrm{WAl}_4} z_r, \tag{5}$$

where V^* is the volume of W consumed per unit volume of WAl_4 formed. Assuming bulk densities, $V^* = 0.198$. Substituting Eq. (5), together with the fact that the sum of the volume fractions f_{Al} and f_{WAl_4} in layer 2 is unity, into Eq. (4) yields

$$\Delta G_s = z_r[\sigma_{\mathrm{Al}}(-1 + V^* f_{\mathrm{WAl}_4}) + (\sigma_{\mathrm{Al}}^{1-f_{\mathrm{WAl}_4}} \sigma_{\mathrm{WAl}_4}^{f_{\mathrm{WAl}_4}}) - \sigma_{\mathrm{W}} V^* f_{\mathrm{WAl}_4}]. \tag{6}$$

The middle term in Eq. (6) can be rewritten as $\sigma_{\mathrm{Al}}(\sigma_{\mathrm{WAl}_4}/\sigma_{\mathrm{Al}})^{f_{\mathrm{WAl}_4}}$ and the term in parenthesis expanded as

$$\left(\frac{\sigma_{\mathrm{WAl}_4}}{\sigma_{\mathrm{Al}}}\right)^{f_{\mathrm{WAl}_4}} = 1 + f_{\mathrm{WAl}_4} \ln\left(\frac{\sigma_{\mathrm{WAl}_4}}{\sigma_{\mathrm{Al}}}\right) + \frac{1}{2}\left[f_{\mathrm{WAl}_4} \ln\left(\frac{\sigma_{\mathrm{WAl}_4}}{\sigma_{\mathrm{Al}}}\right)\right]^2 + \cdots . \tag{7}$$

For small volume fractions of WAl_4, $(\sigma_{WAl_4}/\sigma_{Al})^{f_{\mathrm{WAl}_4}}$ is very well approximated by the first two terms of Eq. (7) with an error that is approximately equal to the third term in which not only is f_{WAl_4} small but $\ln(\sigma_{\mathrm{WAl}_4}/\sigma_{\mathrm{Al}})$ itself is not very large since the conductivities of WAl_4 and Al are comparable. Substituting this result into Eq. (6) yields

$$\Delta G_s = z_r f_{\mathrm{WAl}_4}[\sigma_{\mathrm{Al}} V^* + \sigma_{\mathrm{Al}} \ln(\sigma_{\mathrm{WAl}_4}/\sigma_{\mathrm{Al}}) - \sigma_{\mathrm{W}} V^*]. \tag{8}$$

The kinetics of isotropic diffusion-limited growth have been derived for precipitation from a supersaturated solid solution with the general result being that such precipitates maintain a self-similar shape during growth.[41] In the present case, the WAl_4 particles, from TEM and XTEM micrographs obtained at various stages along the reaction path, also appear to maintain a self-similar shape. Thus, the WAl_4 particle volume is proportional to z_r^3 and $f_{\mathrm{WAl}_4} \propto z_r^3/Az_r \propto z_r^2$, where A is the sample surface area. Using this result, Eq. (8) can be expressed as

$$\Delta G_s = g z_r^3[\sigma_{\mathrm{Al}} \ln(\sigma_{\mathrm{WAl}_4}/\sigma_{\mathrm{Al}}) + (\sigma_{\mathrm{Al}} - \sigma_{\mathrm{W}}) V^*], \tag{9}$$

where g is a geometric factor determined by the average WAl_4 particle shape.

Equation (9) shows that the change in the sheet conductance of our Al/W bilayers during the early stages of annealing should be proportional to the third power of the thickness of the reacted layer, i.e., the third power of the height of WAl_4 particles growing into the Al layer. This is equivalent to saying that the measured sheet conductance is directly proportional to the total volume of unreacted Al. The experimental results presented in Fig. 5 showed that the $\log(-\Delta G_s/G_s^0)$ vs $\log(t_a)$ curves exhibit slopes of approximately 3/2. Thus, from the above model and Eq. (9), the height of the WAl_4 particles increases as $t_a^{1/2}$. Such a parabolic growth law is characteristic of diffusion-limited kinet-

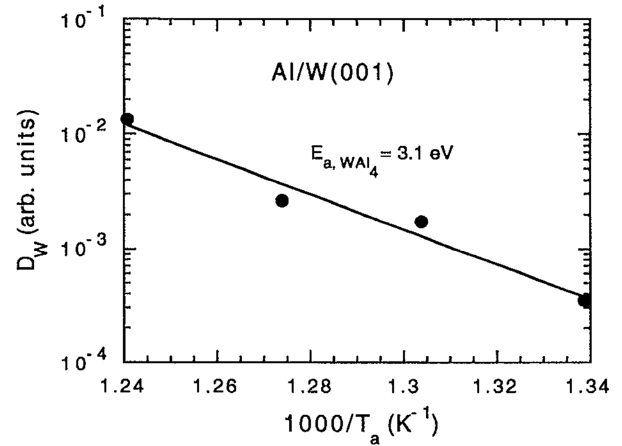

FIG. 14. The diffusion coefficient of W during the formation of WAl_4 in Al/W(001) bilayers as a function of inverse annealing temperature.

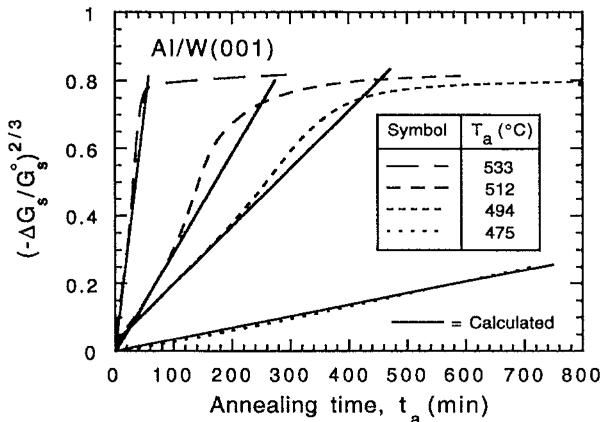

FIG. 13. Normalized decrease in the sheet conductivity to the 2/3 power, $-(\Delta G_s/G_s^0)^{2/3}$, vs time t_a for Al/W(001) bilayers annealed in UHV at $T_a = 475$, 494, 512, and 533 °C.

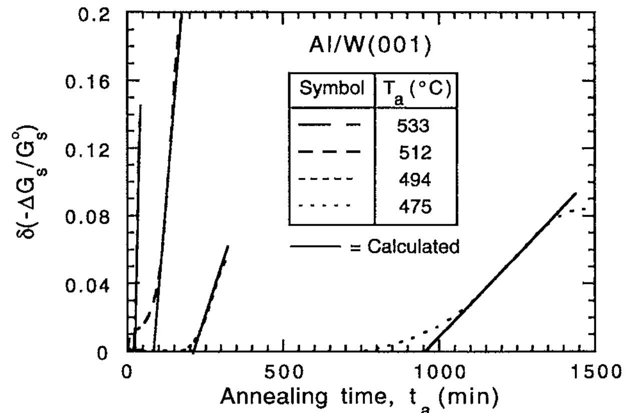

FIG. 15. The deviation of the normalized sheet conductance, $\delta(\Delta G_s/G_s^0)$, from the calculated $t_a^{3/2}$ dependence shown in Fig. 13 for Al/W(001) bilayers annealed at $T_a = 475$, 494, 512, and 533 °C.

Downloaded 30 May 2001 to 130.126.103.205. Redistribution subject to AIP license or copyright, see http://ojps.aip.org/japo/japcr.jsp

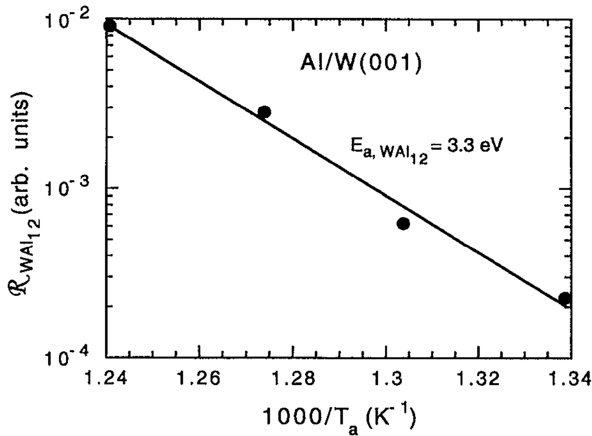

FIG. 16. The formation rate of WAl_{12} in Al/W(001) bilayers as a function of inverse annealing temperature.

ics. The activation energy can now be determined by examining the temperature dependence of the diffusion constant, $D_W \propto z_r^2/t_a$.

Figure 13 is a plot of $(-\Delta G_s/G_s^0)^{2/3}$ vs t_a for four different annealing temperatures between 475 and 533 °C. In each case, there is an initial linear region followed by a positive deviation as the higher aluminide WAl_{12} phase nucleates and begins to grow. From the $\Delta G_s \propto z_r^3$ relationship in Eq. (9), the slopes of the linear regions in Fig. 13 are proportional to the diffusion coefficient of the mobile species—W in this case—at each temperature. The slope of a plot of $\log(D_W)$ vs $1/T_a$, with T_a, in K (Fig. 14), yields an activation energy of 3.1 eV for the diffusion-limited growth of WAl_4.

The growth rate of WAl_{12}, once nucleated, is much higher than that of WAl_4 and, based upon XTEM observations, it grows conformally over both W and WAl_4. Thus, we assume that WAl_{12} and WAl_4 growth kinetics are independent and that the kinetics of WAl_{12} growth can be modeled, following the approach developed above in which the measured sheet conductance is proportional to the volume of unreacted Al in layer 3, by adding an additional phase in layer 2 (see Fig. 12). The change $\delta(\Delta G_s)$ in the differential sheet conductance [Eq. (9)] due to the formation of WAl_{12} is then

$$\delta(\Delta G_s) = (\sigma_{WAl_{12}} + V_{Al}\sigma_{Al} - V_W\sigma_W) z_{WAl_{12}}, \tag{10}$$

where $\sigma_{WAl_{12}}$ is the conductivity of the WAl_{12} layer, V_{Al} and V_W are the volumes of Al and W consumed per unit volume of WAl_{12}, and $z_{WAl_{12}}$ is the thickness of the WAl_{12} layer.

Figure 15 is a plot, based upon the data in Fig. 13, of the deviation of ΔG_s from the initial $t_a^{3/2}$ dependence for several annealing temperatures. The results show that $\delta\Delta G_s$ increases linearly with annealing time. Thus, from Eq. (10), the thickness of the WAl_{12} layer also increases linearly with time indicating that the growth of WAl_{12} is reaction-rate limited rather than diffusion limited as was the case for WAl_4. In this case, the normalized ΔG_s deviation $\delta(\Delta G_s/G_s^0)$ is proportional to the reaction rate $\mathfrak{R}$. Thus, the slope of $\log(\mathfrak{R})$, plotted in arbitrary units in Figure 16, vs $1/T_a$ yields the activation energy which in this case is found to be 3.3 eV.

V. CONCLUSIONS

In summary, we have shown that the reaction of Al/epitaxial-W(001) bilayers during UHV annealing occurs through a two-step process, in which W is the primary mobile species, to consume the entire Al layer. The initial product phase is monoclinic WAl_4 which forms at localized regions along the Al/W interface. WAl_4 is stabilized by a pseudomorphic relationship between high-atom-number planes in the monoclinic phase and the {110} planes of the W underlayer. The growth of WAl_4 is diffusion limited with an activation energy of 3.1 eV. bcc WAl_{12}, whose growth is reaction limited with an activation energy of 3.3 eV, then nucleates at both Al/W, between WAl_4 grains, and Al/WAl_4 interfaces. The WAl_{12} layer grows conformally with essentially uniform thickness to cover the remaining W as well as the WAl_4 grains, which also continue to grow. The surface of the unreacted W remains planar throughout the entire reaction.

It is unclear at this point whether the conclusions previously drawn from Ni marker experiments[23,24] in polycrystalline Al/W bilayers analyzed by RBS alone—that Al is the primary mobile species—are in error or are the result of strongly enhanced Al diffusion down W grain boundaries. We are presently carrying out detailed analyses of annealed polycrystalline Al/W bilayers.

ACKNOWLEDGMENTS

The authors gratefully acknowledge the financial support of the Semiconductor Research Corporation and the Joint Services Electronics Program during the course of this research. We also appreciate the use of the facilities of the Center for Microanalysis, which is partially supported by DOE, at the University of Illinois.

[1] R. S. Nowicki and M.-A. Nicolet, Thin Solid Films **96**, 317 (1982).
[2] C. Y. Ting and M. Wittmer, Thin Solid Films **96**, 327 (1982).
[3] P. B. Ghate, J. C. Blair, C. R. Fuller, and G. E. McGuire, Thin Solid Films **53**, 117 (1978).
[4] J. O. Olowolafe, C. J. Palmstrøm, E. G. Colgan, and J. W. Mayer, J. Appl. Phys. **58**, 3440 (1985).
[5] P.-H. Chang, H.-Y. Liu, J. A. Keenan, J. M. Anthony, and J. G. Bohlman, J. Appl. Phys. **62**, 2485 (1987).
[6] H.-Y. Liu, P.-H. Chang, J. Bohlman, and H.-L. Tsai, Mater. Res. Soc. Symp. Proc. **119**, 153 (1988).
[7] A. S. Bhansali, I. J. M. M. Raaijmakers, R. Sinclair, A. E. Morgan, B. J. Burrow, and M. Arst, Mater. Res. Symp. Proc. **187**, 15 (1990).
[8] A. G. Dirks, R. A. M. Wolters, and A. J. M. Nellissen, Thin Solid Films **193/194**, 201 (1990).
[9] P.-H. Chang, H.-M. Chen, and H.-Y. Liu, J. Appl. Phys. **72**, 2739 (1992).
[10] S. Saito, K. Matsuda, K. Nishizawa, and K. Sakiyama, in *Tungsten and Other Refractory Metals for VLSI Applications II*, edited by E. K. Broadbent (Materials Research Society, Pittsburgh, PA, 1987), p. 319.
[11] B. W. Shen, G. C. Smith, J. M. Anthony, and R. J. Matyi, J. Vac. Sci. Technol. B **4**, 1369 (1986).
[12] P.-H. Chang, R. Hawkins, T. D. Bonifield, and L. A. Melton, Appl. Phys. Lett. **52**, 272 (1988).
[13] C. Canali, G. Celotti, F. Fantini, and E. Zanoni, Thin Solid Films **88**, 9 (1982).
[14] C. Canali, F. Fantini, and E. Zanoni, Thin Solid Films **97**, 325 (1982).
[15] P. Merchant and Jun Amano, J. Vac. Sci. Technol. A **1**, 459 (1983).

Downloaded 30 May 2001 to 130.126.103.205. Redistribution subject to AIP license or copyright, see http://ojps.aip.org/japo/japcr.jsp

[16] R. Furlan, J. Van der Spiegel, and J. W. Swart, J. Electrochem. Soc. **138**, 2377 (1991).
[17] F.-M. Yang and M.-C. Chen, J. Vac. Sci. Technol. B **11**, 744 (1993).
[18] C. J. Palmstrøm, J. W. Mayer, B. Cunningham, D. R. Campbell, and P. A. Totta, J. Appl. Phys. **58**, 3444 (1985).
[19] E. G. Colgan, Mater. Sci. Rep. **5**, 1 (1990).
[20] E. G. Colgan and J. W. Mayer, J. Mater. Res. **4**, 815 (1989).
[21] G. J. van Gurp, J. L. C. Daams, A. van Oostrom, L. J. M. Augustus, and Y. Tamminga, J. Appl. Phys. **50**, 6915 (1979).
[22] I. Krafcsik, J. Gyulai, C. J. Palmström, and J. W. Mayer, Appl. Phys. Lett. **43**, 1015 (1983).
[23] S. Q. Wang and J. W. Mayer, J. Appl. Phys. **67**, 2939 (1990).
[24] S. Q. Wang and J. W. Mayer, Thin Solid Films **207**, 37 (1992).
[25] J. K. Howard, R. F. Lever, P. J. Smith, and P. S. Ho, J. Vac. Sci. Technol. **13**, 68 (1976).
[26] F. Adibi, I. Petrov, L. Hultman, U. Wahlström, T. Shimizu, D. McIntyre, J. E. Greene, and J.-E. Sundgren, J. Appl. Phys. **69**, 6437 (1991).
[27] I. Petrov, F. Adibi, J. E. Greene, W. E. Sproul, and W.-D. Münz, J. Vac. Sci. Technol. A **10**, 3283 (1992).
[28] F. Adibi, I. Petrov, J. E. Greene, L. Hultman, and J.-E. Sundgren, J. Appl. Phys. **73**, 8580 (1993).
[29] R. Powell, G. A. Tomash, Y.-W. Kim, J. A. Thornton, and J. E. Greene, in *Wide Bandgap Semiconductors*, edited by J. T. Glass, N. Fujimori, and R. Messier (Wiley, New York, 1990), p. 25.
[30] L. J. van der Pauw, Philips Res. Rep. **13**, 1 (1958).
[31] R. L. Doolittle, Nucl. Instrum. Methods B **15**, 344 (1985).
[32] J. W. Colby, *Quantex-Ray Instruction Manual* (Kevex, Foster City, CA, 1980).
[33] *Inorganic Index to Powder Diffraction File* (Joint Committee on Powder Diffraction Standards, Pennsylvania, 1993), Card numbers 4-806 (W), 4-829 (MgO), and 4-787 (Al).
[34] H. Kimura, I. Petrov, F. Adibi, and J. E. Greene, J. Cryst. Growth **123**, 344 (1992).
[35] *Metals Handbook*, edited by H. E. Boyer, and L. Gall (ASM, Metals Park, OH, 1985).
[36] See, for example, L. H. Allen, J. W. Mayer, K. N. Tu, and L. C. Feldman, Phys. Rev. B **41**, 8213 (1990).
[37] J. W. Mayer and S. S. Lau, *Electronic Materials Science for Integrated Circuits in Si and GaAs* (MacMillan, New York, 1985), p. 311.
[38] *Phase Diagrams of Binary Tungsten Alloys*, edited by S. B. Nagender Naidu and P. Rama Rao (Indian Institute of Metals, Calcutta, 1991), p. 9.
[39] J. A. Bland and D. Clark, Acta Crystallogr. **11**, 231 (1958).
[40] T. R. Madden, Geophysics **41**, 1104 (1976).
[41] F. S. Ham, J. Phys. Chem. Solids **6**, 335 (1958).

Downloaded 30 May 2001 to 130.126.103.205. Redistribution subject to AIP license or copyright, see http://ojps.aip.org/japo/japcr.jsp